ISPRS Journal of Photogrammetry and Remote Sensing 159 (2020) 129–139

Contents lists available at ScienceDirect

ISPRS Journal of Photogrammetry and Remote Sensing

journal homepage: www.elsevier.com/locate/isprsjprs

Estimation of soil surface water contents for intertidal mudflats using a near-infrared long-range terrestrial laser scanner

Kai Tan[a,*], Jin Chen[a], Weiguo Zhang[a], Kunbo Liu[b], Pengjie Tao[b], Xiaojun Cheng[c]

[a] State Key Laboratory of Estuarine and Coastal Research, East China Normal University, No. 500, Dongchuan Road, Shanghai 200241, China
[b] School of Remote Sensing and Information Engineering, Wuhan University, No. 129, Luoyu Road, Wuhan 430079, China
[c] College of Surveying and Geo-Informatics, Tongji University, No. 1239, Siping Road, Shanghai 200092, China

ARTICLE INFO

Keywords:
Terrestrial laser scanning
Intensity correction
Mudflat
Intertidal zone
Surface soil moisture
Water content

ABSTRACT

Estimations of the soil surface water contents and distributions play a key role in the ecological, environmental, and topographical investigations for intertidal mudflats. However, existing techniques have limitations. Long-range terrestrial laser scanners (TLSs) can record the co-located intensity value which refers to a measure of the backscattered laser from each scanned point. Most long-range TLSs emit near-infrared lasers that can be strongly absorbed by water. Thus, the intensity values can be used as proxies for water contents. In this study, the intensity data of long-range TLSs are corrected for the incidence angle and distance effects to quantitatively estimate the soil surface water contents of intertidal mudflats. A case study for a mudflat in Chongming Island, Shanghai, China, is conducted. Results indicate that compared with traditional techniques, the corrected intensity data of long-range TLSs are extremely effective data sources for a quick, accurate, and detailed estimation of water contents for large-area mudflats. The estimation root mean square error is approximately 3%. Furthermore, the 3D distributions of the water contents can be accurately mapped by combining the point cloud of the mudflats to potentially analyze the intrinsic association among water contents and topography, vegetation coverage, and habitation of creatures in mudflats.

1. Introduction

Mudflats (i.e., tidal flats) are nearly flat coastal areas in intertidal zones that are considered the transitions and hubs between ocean and land. Materially, mudflats consist of unconsolidated sediments and precipitated salts and are characteristically wet and periodically submerged by sea water (Eisma, 1998; Le Hir et al., 2000; Wang et al., 2012). Geologically, mudflats can be viewed as exposed layers of bay mud that are resulted from the deposition of estuarine silts, clays, and marine animal detritus. From the environmental and ecological perspectives, mudflats shelter a myriad of ecological niches and provide valuable habitats for creatures, including microorganisms, worms, crabs, sand fleas, birds, and fishes (Choe et al., 2012; Phang et al., 2015). Thus, a detailed investigation of mudflats is beneficial to the geomorphological, hydrological, ecological, environmental, and hydrodynamic research in intertidal zones. The distribution and variation of soil surface water contents (moistures) are key parameters in the investigation of mudflats. Water content estimation is important for the comprehensive understanding of the formation, transportation, movement, and material exchange mechanisms of a mudflat (Brakenhoff et al., 2019; Nield et al., 2011; Nield and Wiggs, 2011; Schmutz and Namikas; 2018; Smit et al., 2019; Oblinger and Anthony, 2008). Furthermore, water is necessary for the creatures that live in mudflats. Water contents have a notable impact on the habitation, migration, and metabolism of these creatures. Given the effects of infiltration and gravity, water contents are closely related to the topography of a mudflat (Li et al., 2018).

Traditionally, several representative samples are manually collected, weighted, and dried at indoor environments for the calculation of water contents of a mudflat (i.e., gravimetric method). Another conventional method is to use in situ water content measurement probes, e.g., Delta-T theta probe, commercial soil moisture sensors (Schmutz and Namikas, 2011; Edwards et al., 2013; Wiggs et al., 2004; Yang and Davidson-Arnott, 2005). The use of traditional methods is laborious, destructive, and time consuming. Periodic flooding, dense vegetation, and muddy environments make the mudflats usually human-inaccessible (Xie et al., 2017). Traditional methods require direct contact to the mudflats, thereby placing data collectors in danger.

* Corresponding author.
E-mail addresses: ktan@sklec.ecnu.edu.cn (K. Tan), 51173904002@stu.ecnu.edu.cn (J. Chen), wgzhang@sklec.ecnu.edu.cn (W. Zhang), liukunbo@whu.edu.cn (K. Liu), pjtao@whu.edu.cn (P. Tao), cxj@tongji.edu.cn (X. Cheng).

https://doi.org/10.1016/j.isprsjprs.2019.11.003
Received 20 July 2019; Received in revised form 2 November 2019; Accepted 5 November 2019
Available online 26 November 2019
0924-2716/

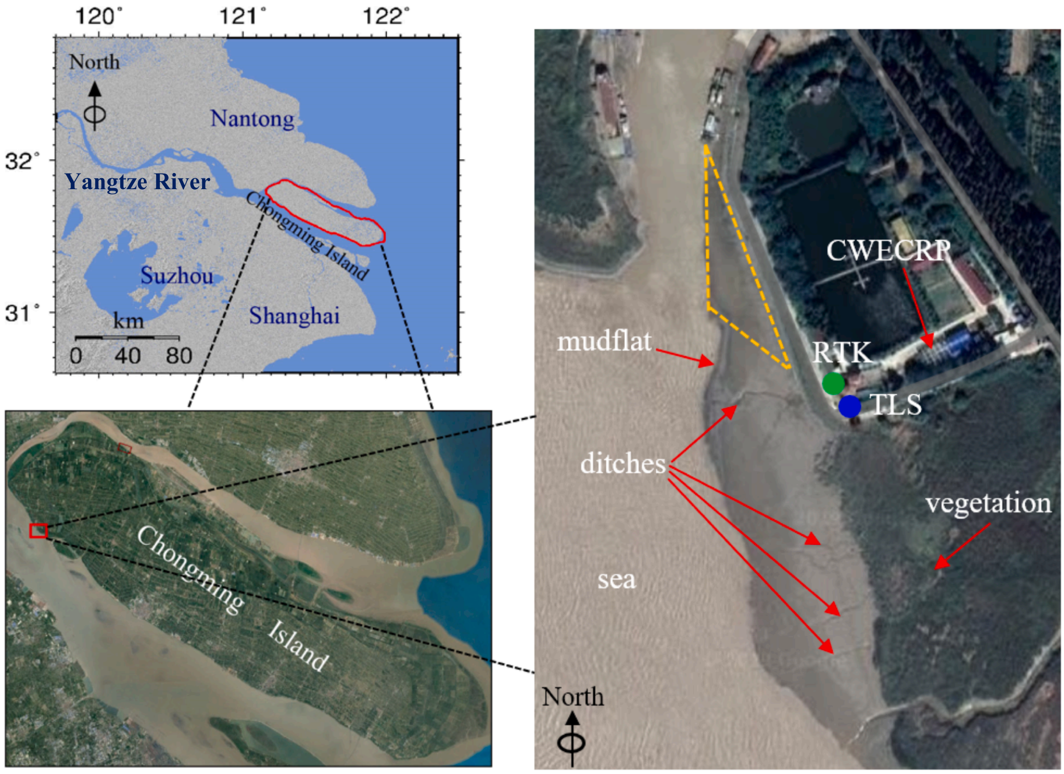

Fig. 1. Location of the study mudflat. The orthophoto of the mudflat was provided by Google Earth (http://www.google.cn/maps). Riegl VZ-4000 TLS and Trimble R8 RTK reference station were positioned at the blue and green points, respectively. The north corner of the mudflat (yellow dotted frame) cannot be scanned by the TLS. (For interpretation of the references to color in this figure legend, the reader is referred to the web version of this article.)

Moreover, limited sparse samples from traditional methods cannot obtain a detailed presentation of water distributions. Technological advancements have introduced various alternative techniques for the water content investigation of mudflats. Particularly, remote sensing techniques can estimate the water contents of large-area mudflats in a noncontact way using an extremely narrow and continuous spectral channel (Darke et al., 2009; Nolet et al., 2014; Rajput et al., 2018). However, remote sensing images are subjected to the environment, such as sunlight, atmosphere, and cloud. Also, only two-dimensional (2D) information can be provided by remote sensing images, and the spatial resolutions of remote sensing images are insufficient for the investigation of the microtopographic-scale water content variations. Therefore, existing techniques cannot adequately characterize the spatiotemporal distribution of surface water contents of mudflats.

In the past two decades, terrestrial laser scanners (TLSs) have been widely used in investigating the detailed geomorphological characteristics of perennial inaccessible intertidal mudflats because of its advantages of being contactless, high precision, and high resolution (Andriolo et al., 2018; Guisado-Pintado et al., 2019; Nahon et al., 2019; Nguyen et al., 2018; Telling et al., 2017). The advantage of TLSs over other surveying techniques is that TLSs can provide accurate and dense sets of 3D coordinates of scanned objects in a rapid and noninvasive manner by firing monochromatic beams of light to determine the distances (ranges) between the scanned points and the scanner center. TLSs can reflect detailed geomorphological features and present new perspectives in the investigation of mudflats by using a high-density point cloud (Xie et al., 2017; Donker et al., 2018; Fabbri et al., 2017). In addition to the 3D geometrical measurements, TLSs can simultaneously measure the power of the backscattered laser signal reflected by each point. Backscattered optical power is internally converted to voltage, amplified in the system, and finally transformed into a digital number called intensity (Höfle and Pfeifer, 2007; Kaasalainen et al., 2011; Kashani et al., 2015). The power of the backscattered laser depends on the reflectance of the scanned target. Therefore, intensity value is closely related to the target reflectance. Most TLS systems operate in the near-infrared spectrum, where infrared laser light can be strongly absorbed by water. Even a limited amount of water has a crucial effect on the reflectance properties of the target (Tan et al., 2016). Thus, the intensity data can be used theoretically to derive the soil surface water contents of mudflats. However, the original intensity data are significantly affected by the incidence angle between beam propagation direction and surface orientation, and the distance (range) between the scanner center and the measured point (Xu et al., 2017; Tan and Cheng, 2015; Fang et al., 2014). The elimination of the effects of distance and incidence angle is indispensable for deriving water contents from the intensity data.

TLSs can be classified into short-, middle-, and long-range scanners based on their ranging capability. The maximum measured distances for short- and middle-range TLSs are limited; hence, these TLSs are not suitable for the data collection of large-area mudflats. On the contrary, long-range TLSs can rapidly obtain point cloud from several meters up to kilometers with near-centimeter precision (Tan et al., 2019). This technology is especially suitable for large-area topographical data acquisition. To date, TLS intensity data are proven effective data sources in estimating the water contents of different targets, e.g., metro/underground tunnels (Tan et al., 2016; Xu et al., 2018), building materials (Suchocki and Katzer, 2018), and tree leaves (Zhu et al., 2015). The water contents of the aforementioned targets are relatively low (<20%). Additionally, several researchers have already attempted to utilize the distance effect corrected intensity data of short-range (e.g., Leica Scanstation) and middle-range (e.g., Riegl VZ-400) TLSs for the water content estimation of aeolian sandy beaches (Nield and Wiggs, 2011; Nield et al., 2011, 2014; Nolet et al., 2014; Smit et al., 2018). The water contents of intertidal mudflats are generally higher than those of the sandy beaches. Thus, the estimation model for sandy beaches may not be suitable for mudflats. Moreover, apart from the distance effect, the incidence angle has a critical effect on the intensity data; hence, this effect should also be considered to improve the accuracy of water content estimation (Poullain et al., 2016). In contrast with existing studies, this study adopts a long-range TLS (Riegl VZ-4000) to collect the 3D point cloud and intensity data of a mudflat in Chongming Island, Shanghai, China. Intensity data are corrected for the incidence angle and distance effects by combining indoor control experiments and naturally homogeneous targets to estimate the soil surface water contents and distributions of the mudflat. The remainder of this paper is organized as follows. Section 2 reviews the instruments used and the chosen study site. Section 3 outlines the methodology for mudflat water content estimation using the corrected intensity data of long-range TLSs. Sections 4 and 5 present the results and discussions, respectively. Section 6 presents the conclusions of this study.

2. Study site and instruments

2.1. Study site

An intertidal mudflat (N 31.73°, E 121.22°) located on Chongming Island, Shanghai, China, was selected as the study site for this work (Fig. 1). Chongming Island is located at the mouth of the Yangtze River, and it is the largest estuary alluvial island and the largest sand island in China. The mudflat that runs from north to south is located on the southwest corner of Chongming Island. The elevation of the mudflat gradually rises from north to south and varies slightly from east to west. The mudflat is long and narrow with a size of approximately 500 m × 100 m. The mudflat is composed of soft clay and silt. Thus, walking on it is extremely difficult. The muddy depth varies from 0.1 m to 0.5 m. The mudflat surface is bare, that is, it does not have vegetation coverage. Dense reeds and other salt-tolerant plants grow in salt-marshes on the east side of the mudflat. The height of these vegetations is approximately 1.0–2.0 m. Several tidal ditches that run from east to west are distributed among the mudflat. The width of the ditches is approximately 0.5–3.0 m. The sea is located on the west side of the mudflat. Chongxi Wetland Ecological Construction Research Project Office (CWECRPO) is located on the northeast corner. Narrow cement roads, which facilitate the access to the mudflat, are found around the CWECRPO.

2.2. Instruments and data collection

A Riegl VZ-4000, which is a pulsed TLS system with remarkable ranging capability that can measure distances from 5 m to 4000 m, was adopted as the scanner in this study. Its vertical and horizontal field of views are 360° and 60°, respectively. The intensity value for each single point is recorded in decibel (dB), which is a logarithmic unit that indicates the ratio of a physical quantity (usually power or intensity) relative to a specified or implied reference level and does not have any physical meaning. Therefore, intensity data are dimensionless. Also, Riegl VZ-4000 can theoretically measure distance of up to 4000 m. However, the largest distance capability is achieved under specific conditions (e.g., perpendicular incidence angle, flat target larger than the footprint of the laser beam, 90% target reflectance, and standard clear atmosphere). In actual scans, the maximum measured distance is considerably less than 4000 m (Tan et al., 2019). Empirically, the analysis of different field data acquired by Riegl VZ-4000 shows that the scanned data at long distances are sparse and unreliable. Similar to Tan et al. (2019), the present study disregarded the data with distances longer than 500 m to ensure good reliability and quality of the point cloud.

The mudflat was scanned by the Riegl VZ-4000 on June 6, 2018, when was sunny and windless. The Riegl VZ-4000 was positioned on the cement road at the southwest corner of the CWECRPO (blue point in Fig. 1). The scanning survey began from 11:30 a.m. and ended at 12:10 p.m., which was exactly within the low tide time. The scanning field of view was set to the default state. The vertical and horizontal angle resolutions were set to 0.02° and 0.03°, respectively. The pulse repetition rate was fixed as 30 kHz. In this study, the scanning parameters of Riegl VZ-4000 were kept unchanged for all the experiments. The preprocessing of the point cloud data was conducted using the standard software RiSCAN PRO v1.8.1 (RIEGL Laser Measurement Systems GmbH, Horn, Austria). The point cloud of the mudflat was then exported to MATLAB for intensity correction and water contents estimation by using developed algorithms that were introduced in Section 3.

2.3. Mudflat sampling

After data collection using Riegl VZ-4000, several samples of the mudflat were immediately collected for the following purposes: (1) to quantitatively estimate the relationship between water contents and corrected intensity data, and (2) to validate the accuracy of the estimation model. The size of each sample was approximately 10 cm × 10 cm, and their thickness was approximately 3–5 cm. Each sample was stored in a sealed plastic bag. A total of 48 samples were evenly collected throughout the mudflat. The water contents of the field samples were measured in a laboratory using the gravimetric method (Nield et al., 2011; Smit et al., 2018), which was in detail introduced in Section 3.3. To determine the accurate positions of the samples in the point cloud during postprocessing, a Trimble R8 GNSS RTK system was used as an auxiliary tool to measure the positions of the centers of the field samples. The Trimble R8 reference station was placed at approximately 3 m nearby the TLS (green point in Fig. 1). The height of the Trimble R8 reference station was 1.80 m. The horizontal and vertical accuracies of the RTK system were 0.01 m and 0.02 m, respectively.

3. Methods

3.1. Intensity correction

TLS intensity is a measure of the electronic signal strength that is obtained by converting and amplifying the backscattered optical power of the emitted signal (Tan and Cheng, 2015). The TLS intensity data correction has been widely investigated in the past ten years, and many different correction methods have been proposed (Fang et al., 2014; Franceschi et al., 2009; Kaasalainen et al., 2009; Kaasalainen et al., 2011; Kashani et al., 2015; Tan and Cheng, 2015; Tan et al., 2016; Tan and Cheng, 2016; Xu et al., 2017; Yan and Shaker, 2014). Intensity correction for long-range TLSs are limited by the length limit of indoor environments and the laborious data acquisition and processing work (Tan et al., 2019). In this study, the intensity data of Riegl VZ-4000 were corrected using the method in Tan et al. (2019).

Given that all sensor-related factors are kept constant during the campaign, and the atmospheric transmission effect can be neglected, the intensity data obtained by a TLS system are merely influenced by target reflectance, incidence angle, and distance. The original intensity data can be expressed as (Tan and Cheng, 2015; Tan et al., 2019):

$$I = f_1(\rho)\bullet f_2(\theta)\bullet f_3(d) \quad (1)$$

where f_1, f_2, and f_3 are the functions of target reflectance ρ, incidence angle θ, and distance d, respectively. The incidence angle and distance are derived as follows:

$$\begin{cases} \theta = cos^{-1}\left|\frac{\boldsymbol{OS}\cdot\boldsymbol{n}}{d\cdot|\boldsymbol{n}|}\right| \\ d = \sqrt{(x-x_0)^2+(y-y_0)^2+(z-z_0)^2} \end{cases} \quad (2)$$

where $\boldsymbol{n} = (n_1, n_2, n_3)$ is the surface normal vector implemented by computing the best-fitting plane with the available data on the nearby neighborhood of each measured laser point. The incidence laser radiation vector $\boldsymbol{OS} = (x - x_0, y - y_0, z - z_0)$ is calculated using the original geometrical coordinates (x, y, z) of the scanned point and the coordinates (x_0, y_0, z_0) of the scanner center.

The corrected intensity (I_s) that is merely related to the target reflectance can be written as:

$$I_s = f_1(\rho)\bullet f_2(\theta_s)\bullet f_3(d_s) \tag{3}$$

where $f_2(\theta_s)\bullet f_3(d_s)$ is a constant, and θ_s and $\mathrm{d_s}$ are the reference incidence angle and distance, respectively. According to Tan and Cheng (2015), $f_2(\theta)$ and $f_3(d)$ can be empirically approximated by a polynomial regardless of the internal details of the instrumental mechanisms, that is, $f_2(\theta) = \sum_{i=0}^{N_2}(\alpha_i\theta^i)$ and $f_3(d) = \sum_{i=0}^{N_3}(\beta_i d^i)$, where N_2, α_i, N_3, and β_i are polynomial parameters. Therefore, the corrected intensity is obtained by dividing Eqs. (1) and (2) (Tan and Cheng, 2015; Tan et al., 2019):

$$I_s = I\bullet\frac{f_2(\theta_s)\bullet f_3(d_s)}{f_2(\theta)\bullet f_3(d)} = I\bullet\frac{\sum_{i=0}^{N_2}(\alpha_i\theta_s^i)\bullet\sum_{i=0}^{N_3}(\beta_i d_s^i)}{\sum_{i=0}^{N_2}(\alpha_i\theta^i)\bullet\sum_{i=0}^{N_3}(\beta_i d^i)} \tag{4}$$

Eq. (4) was used to calculate the corrected intensity data for Riegl VZ-4000 in the present study. The polynomial parameters were estimated, as introduced in Section 3.2.

3.2. Estimation of polynomial parameters

To estimate the polynomial parameters of $f_2(\theta)$ for Riegl VZ-4000, four different homogeneous targets were pasted on a board (Fig. 2(a)). The board could be rotated and was scanned at a fixed distance of 7.5 m from the scanner at indoor environments. The incidence angle of the board was nearly changed from 0° to 85° in steps of 5°. The board was scanned in each orientation step. The point clouds of the four targets scanned in the laboratory at each orientation step were manually sampled and exported in RiSCAN PRO v1.8.1. The mean incidence angle and original intensity over all the sampled points of the four reference targets were used for the analysis. Given this circumstance, d_x was unchanged. The reflectance values of the homogeneous reference target were unknown, but were the same for all the points of the homogeneous reference target. Therefore, ρ_x and d_x can be considered constants; $f_1(\rho)$ and $f_3(d)$ in Eq. (1) were changed into constants. Hence, the original intensity I was merely related to the incidence angle θ. N_2 and α_i can be estimated by analyzing the scanned data of the homogeneous reference targets.

In the present study, a cement road on a seawall was selected to derive the parameters of $f_3(d)$ for Riegl VZ-4000 (Fig. 2(b)). The incidence angle-corrected intensity I_a of the cement road was calculated by using the derived parameters of $f_2(\theta)$ in the first step. The reflectance (ρ_y) was unknown but constant for the cement road. The incidence angle-corrected intensity I_a of the road did not depend on the incidence angle. Thus, I_a was merely related to distance. N_3 and β_i can be estimated by analyzing the relationship between the incidence angle-corrected intensity and distance of the cement road using a least squares adjustment method. The cement road from the three different sites were scanned to reduce possible errors or noises in one scanning campaign.

3.3. Estimation of water contents using corrected intensity data

The coordinate system of Riegl VZ-4000 is the local instrumental system; whereas RTK adopts the WGS84 coordinate system. To match the two different data sources acquired by TLS and RTK, five special-made plastic targets (Fig. 2(c)) were used to provide both translation and rotation parameters between the two coordinate systems. A circle reflective sheet was pasted on the center of each plastic target. The plastic targets were mounted on tripods, and the tripods were set up around the scanner with a detecting range of 50–100 m in the study area. Riegl VZ-4000 scanned the point cloud of the circle reflective targets. RiSCAN PRO automatically identified and extracted the point cloud and calculated the 3D coordinates of the centers of the circle reflective sheets. The positions and elevations (WGS84 coordinates) of the centers of these five reflective sheets were also measured using the RTK. The RTK receiver was placed on the top cylinder of the plastic targets (Fig. 2(c)). Additionally, the WGS84 coordinates of several feature points (e.g., building corners, junction points between pole and ground) were measured, and the feature points were manually found in the point cloud. The translation and rotation parameters between the RTK and TLS coordinate systems were calculated using the two sets of coordinates from the centers of five circle reflective sheets and feature points. Therefore, the positions of the centers of the collected samples measured by the RTK could be transformed into the instrumental coordinates of Riegl VZ-4000. Fig. 2(d) indicates the corresponding nearest points to the center of the samples in the point cloud. The neighbor points (10 cm × 10 cm) around the corresponding nearest points were manually selected, and the mean intensity values of the neighbor points were used for analysis. This scenario corresponded to the fact that the field samples were 10 cm × 10 cm, and the mean intensity values of the field samples were adopted.

The field samples were taken back to the laboratory for water content measurement. First, the weights (W_0) of the field samples were measured using a precise electronic scale (MP 200A, accuracy: ±0.001 g). The field samples were taken out for weighing again by heating under 105℃ for 24 h in an oven (Nield et al., 2011; Smit et al., 2018). Currently, the field samples were assumed to contain no water, and the weights of the field samples were W_1. Thus, the water contents of the field samples were calculated as:

$$W = \frac{W_0 - W_1}{W_0} \times 100\% \tag{5}$$

Some dry mud was taken from the field samples and was placed in a plastic plate (size: 10 cm × 10 cm × 3 cm). Then, the mud was evenly

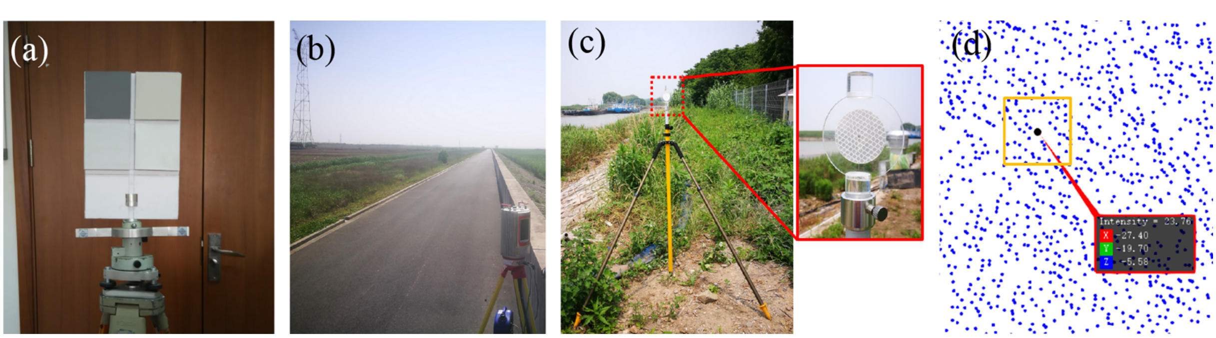

Fig. 2. (a) Four different homogeneous targets. (b) A cement road. (c) One of the plastic targets used to match the data acquired by Riegl VZ-4000 and Trimble R8 GNSS RTK. A circle sheet made of reflective material was pasted on the center of the planar target. (d) Calculation of the corrected intensity values for the field samples. The black point was the nearest point to the sample. The mean corrected intensity value of the points within the yellow rectangle (10 cm × 10 cm) was used. (For interpretation of the references to color in this figure legend, the reader is referred to the web version of this article.)

Table 1
Polynomial parameters and standard deviations.

N_2	$\alpha_0/\sigma_{\alpha_0}$	$\alpha_1/\sigma_{\alpha_1}$	$\alpha_2/\sigma_{\alpha_2}$	$\alpha_3/\sigma_{\alpha_3}$
3	1.00/0.14	-3.38×10^{-3}/0.73	2.4×10^{-5}/1.2	-9.73×10^{-7}/0.50
N_3	β_0/σ_{β_0}	β_1/σ_{β_1}	β_2/σ_{β_2}	β_3/σ_{β_3}
7	-7.49×10^{-2}/0.84	2.55/0.62	27.6/1.4	140.0/1.4
β_4/σ_{β_4}	β_5/σ_{β_5}	β_6/σ_{β_6}	β_7/σ_{β_7}	
−377.5/1.9	552.08/0.74	−394.4/1.8	1.00/0.22	

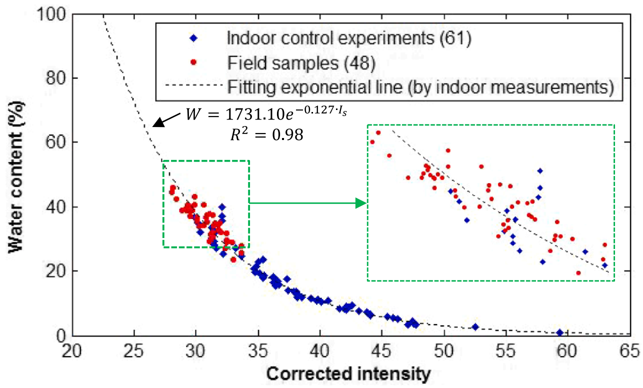

Fig. 3. Relationship between the corrected intensity and water content.

stirred with water to make a new sample. The dry mud and added water were weighted using the MP 200A electronic scale; hence, water content of the new sample was determined. The initial water content of the new sample was basically saturated (approximately 40%). Subsequently, the Riegl VZ-4000 was used to scan the new sample, and the distance between the scanner and the new sample was approximately 10 m. Afterwards, the new sample was placed into the oven for several minutes (15–30 min). Finally, the new sample was taken out for weighting and scanning using the Riegl VZ-4000 again. The water contents ($W^{'}$) of the new sample and their corresponding original intensity data were obtained by repeating the aforementioned steps until the new sample became dry. The original intensity data were corrected by using Eq. (4) to determine the corrected intensity data. The point clouds of the new sample at each scan were manually sampled and exported in RiSCAN PRO v1.8.1. The mean original intensity over all the sampled points of the new sample was used for the analysis. In this study, the datasets of the new sample were used for estimating the relationship between the corrected intensity data and water contents because the changes in the water contents of the new sample were more continuous and controllable than that of the field samples. On the contrary, the datasets of the field samples were used to validate the accuracy of the estimation model.

Eq. (3) shows that the corrected intensity data are merely related to reflectance. The water would absorb the laser and reduce the reflectance of the mudflat. Therefore, corrected intensity data could be used to quantitatively estimate the water content, as shown by Eq. (6).

$$W^{'} = F(I_s) \tag{6}$$

where $W^{'}$ is the water content, and F is a monotonically decreasing function of I_s. The specific form of F can be determined by mathematically analyzing the relationship between the corrected intensity data and water contents of the new sample. Considering that water contents decrease with the corrected intensity data, and the corrected intensity would be infinitely close to a constant when the water content trends to 0%, an exponential function (Eq. (7)) was used to fit the relationship between the corrected intensity and water contents in this study, similar to the studies of Nield et al. (2011, 2014), and Smit et al. (2018).

$$W^{'} = \varphi_1 \bullet e^{\varphi_2 \bullet I_s} \tag{7}$$

where φ_1 and φ_2 are two parameters. By conducting a logarithm operation on the two sides of Eq. (7), we can obtain

$$L = X_1 + X_2 \bullet I_s \tag{8}$$

where $L = log_e(W^{'})$, $X_1 = log_e(\varphi_1)$, and $X_2 = \varphi_2$ (e is the natural base). By a least squares adjustment of Eq. (8), parameters X_1 and X_2 can be estimated as $[X_1, X_2]^T = (B^T \bullet B)^{-1} \bullet B^T \bullet L$, where $B = [1, I_s]$. Thus, $\varphi_1 = e^{X_1}$ and $\varphi_2 = X_2$. After obtaining φ_1 and φ_2, the water contents of the mudflat can be calculated using Eq. (7) based on the corrected intensity data.

4. Results

4.1. Polynomial parameters estimation for TLS intensity correction

The third- and seventh-degree polynomials were used to fit the relationships of the incidence angle-intensity and distance-intensity by testing different orders of polynomials and comparing the fitting accuracy, respectively. Table 1 presents the mean values and the standard deviations (σ) of the polynomial parameters of $f_2(\theta)$ and $f_3(d)$. The detailed methods and procedures for polynomial parameter estimation for Riegl VZ-4000 can be found in Tan et al. (2019).

4.2. Relationship between corrected intensity data and water contents

In this study, the reference incidence angle (θ_s) and distance (d_s) were defined as 30° and 10 m, respectively. A total of 61 datasets of the new sample were obtained at indoor environments. The water contents of the new sample varied from 40% (nearly saturated) to 1% (nearly dry). The blue points in Fig. 3 shows the relationship between the water contents and the corrected intensity data of the new sample measured at indoor environments. Water contents significantly decreased from 40% to 8% with the increase in the corrected intensity data from 30 to 45. Water contents slightly decreased when intensity increased from 45 to 60. By a least squares adjustment of Eq. (8) using the datasets of the new sample, φ_1 and φ_2 were estimated as 1731.10 ($\sigma_{\varphi_1} = 0.09$) and − 0.127 ($\sigma_{\varphi_2} = 0.24 \times 10^{-2}$), respectively, and the correlation-coefficient squared (R^2) was 0.98. Additionally, the red points in Fig. 3 present the water contents and corrected intensity data of the 48 field samples collected on site. The water contents of the field samples varied from 24% to 48%. Apparently, the red points fitted well with the exponential line estimated by the new sample scanned at indoor control experiments. This result indicates that good consistency existed between the indoor and outdoor measurements. The result also suggests that the exponential model can be used to accurately fit the relationship between the corrected intensity and the water contents of the mudflat.

4.3. Estimation of mudflat water contents using corrected intensity data

Given the occlusion by several vegetation and artificial facilities, the northwest corner of the mudflat cannot be scanned by Riegl VZ-4000

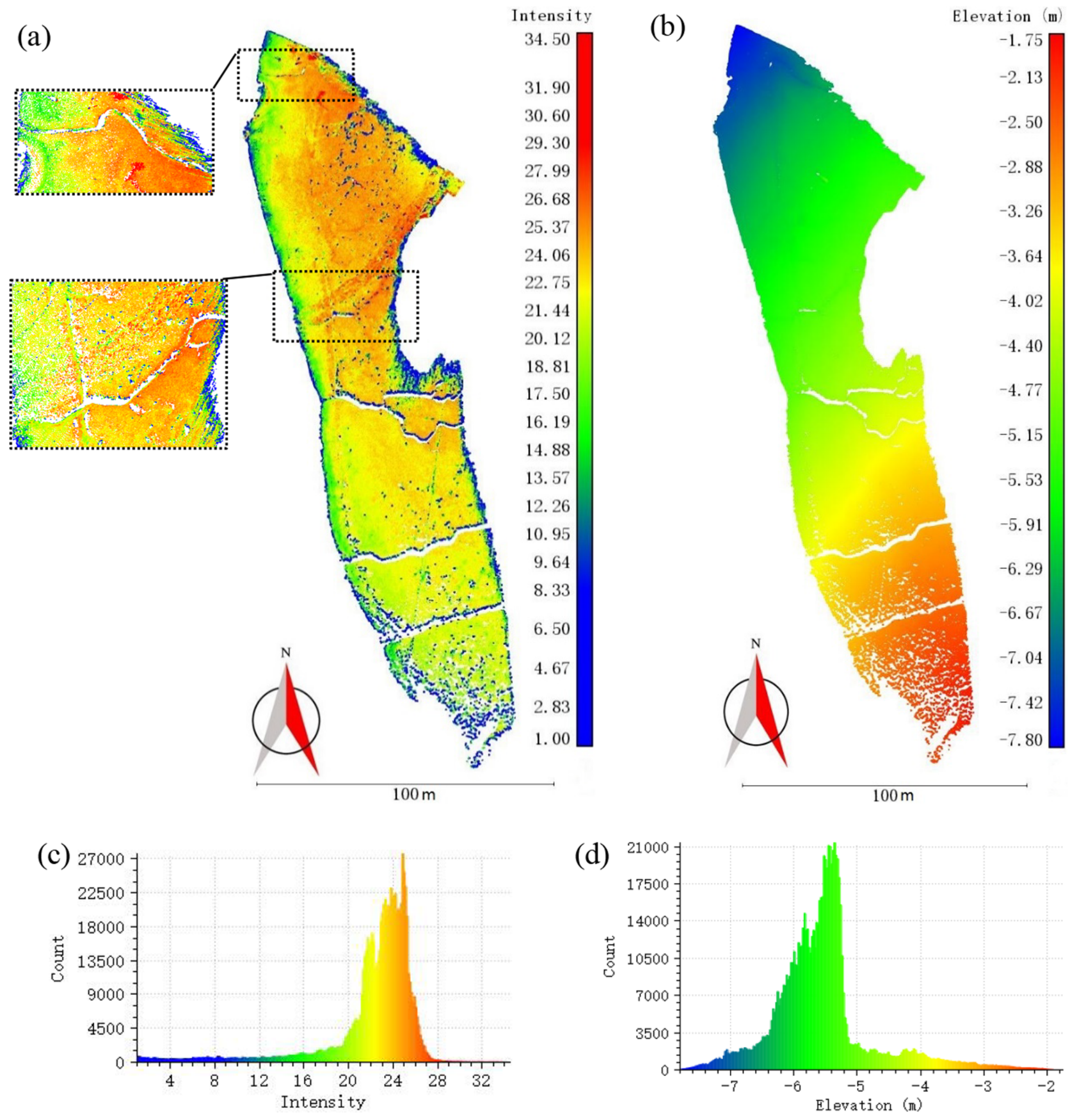

Fig. 4. (a) Point cloud of the study mudflat colored by original intensity data, (b) Point cloud of the study mudflat colored by height/elevation, (c) Histogram of the original intensity data, (d) Histogram of the height/elevation.

(yellow dotted frame in Fig. 1). A total of 848,439 points were obtained for the mudflat. The average point density was approximately 30 points/m^2. Fig. 4(a) shows the point cloud of the mudflat (300 m × 100 m) colored by the original intensity data. The original intensity data of the mudflat varied from 1 to 35. Generally, the intensity values of the northern part were larger than those of the southern part. On the contrary, no significant differences in the intensity values from the eastern to western directions were observed. Fig. 4(b) shows the point cloud of the mudflat colored by the elevation (height). The elevation gradually decreased from the southern to the northern parts of the mudflat. The southern part was approximately 6 m higher than that of the northern part, and the slope angle at the south to north directions was approximately 1.4°.

The corrected intensity data of the mudflat were calculated by using Eq. (4) according to the parameters listed in Table 1. Fig. 5(a) shows the point cloud of the mudflat colored by the corrected intensity data. The corrected intensity data of the mudflat varied from 25 to 40. Small intensity values (blue points) were found at the borders around the mudflat. Fig. 5(b) shows the water contents of the mudflat that were estimated by substituting the corrected intensity data into Eq. (7). The water contents of the mudflat ranged from 12% to 65%, and most of the water contents were distributed from 25% to 40%. Evidently, the water contents of the northern part were generally higher than those of the southern part.

Fig. 5(d) shows that most of the water contents for the mudflat were between 25% and 40%. Only a small part of the regions had water contents larger than 40% or smaller than 25%. Thus, the water contents were divided into three different levels in this study: 12–25% (low), 25–40% (middle), and 40–65% (high), as shown by Fig. 6. Most regions with low level water contents were located in the southern part; by contrast, most regions with middle level water content lied at the northern part. Regions with high level water contents appeared at the boundaries of the mudflat, the two banks of the ditches, and the edges of local low-lying areas (e.g., crab caves). For a clear and detailed presentation, water contents of the mudflat were segmented into 10 different sections. Each section was represented by a different color; thus, the local changes of water contents could be clearly reflected (Fig. 6(d)).

The water contents of the 48 field samples measured by gravimetric method and estimated by Eq. (7) were compared (Fig. 7). The minimum and maximum root mean square errors (RMSE) were 0.41% and 5.29%, respectively. The average RMSE for the 48 samples was 2.93%,

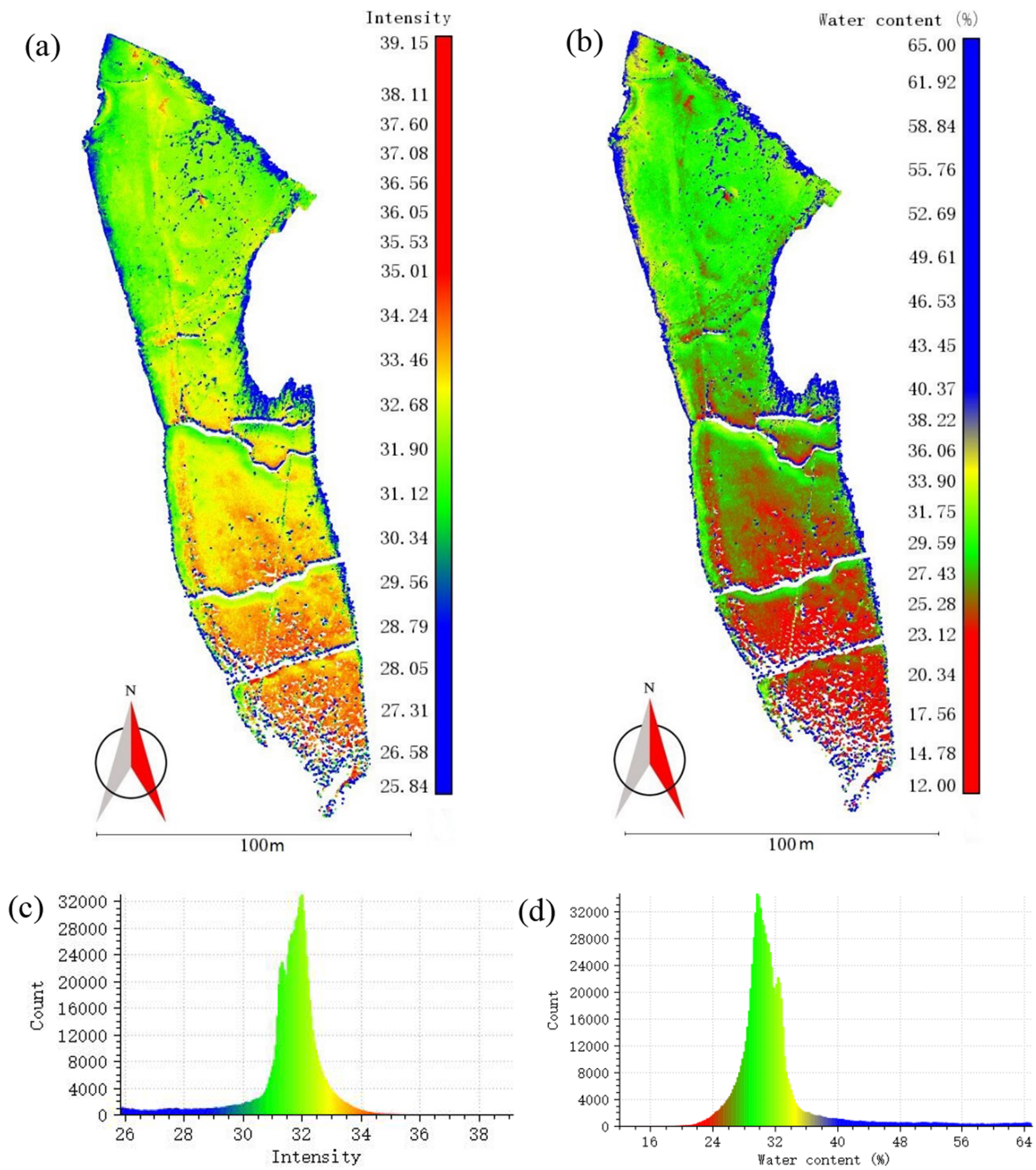

Fig. 5. (a) Point cloud of the study mudflat colored by corrected intensity data, (b) Point cloud of the study mudflat colored by water content, (c) Histogram of the corrected intensity data, (d) Histogram of the water contents.

indicating that the corrected intensity data of Riegl VZ-4000 can be used to estimate the water contents of the mudflat with an error of approximately 3%. The accuracy obtained in this study was very similar to that obtained using the theta probes with a RMSE of ±2% (Schmutz and Namikas, 2011), optical brightness with a RMSE on the order of 3–4% (Darke et al., 2009), and corrected intensity data of middle-range TLS (Riegl VZ-400) with a RMSE of 2.7% (Smit et al., 2018).

The photos taken on site and the corresponding water contents derived by Riegl VZ-4000 were compared in Fig. 8. The water contents and geomorphology of most local low-lying areas can be recorded, indicating the effectiveness and high-accuracy of the proposed method. All the emitted lasers were absorbed by water, and no signal was detected by the TLS when the stagnant water reached a certain amount. Hence, Fig. 8 shows that no points could be obtained in some of the regions with stagnant water. However, reflected signals may still appear when the amount of stagnant water is not high.

5. Discussion

5.1. Intensity data correction

Theoretically, the intensity data of the Riegl VZ-4000 are also influenced by atmospheric conditions (e.g., temperature, humidity, and pressure), instrumental mechanism, and target surface roughness (Fang et al., 2014; Höfle and Pfeifer, 2007; Xu et al., 2017; Tan et al., 2019). The TLS instrumental configurations are always kept constant. The atmospheric conditions near the surface of the Earth are relatively stable; hence, the atmospheric attenuation on TLS intensity data can be ignored. Additionally, the mudflat is composed of soft clay and silt; thus, the difference in surface roughness is subtle. Moreover, the parameters of $f_2(\theta)$ estimated by the four homogeneous targets are used to correct the incidence angle effect on the intensity data of the cement road and mudflat. Strictly speaking, the incidence angle effect is related to the

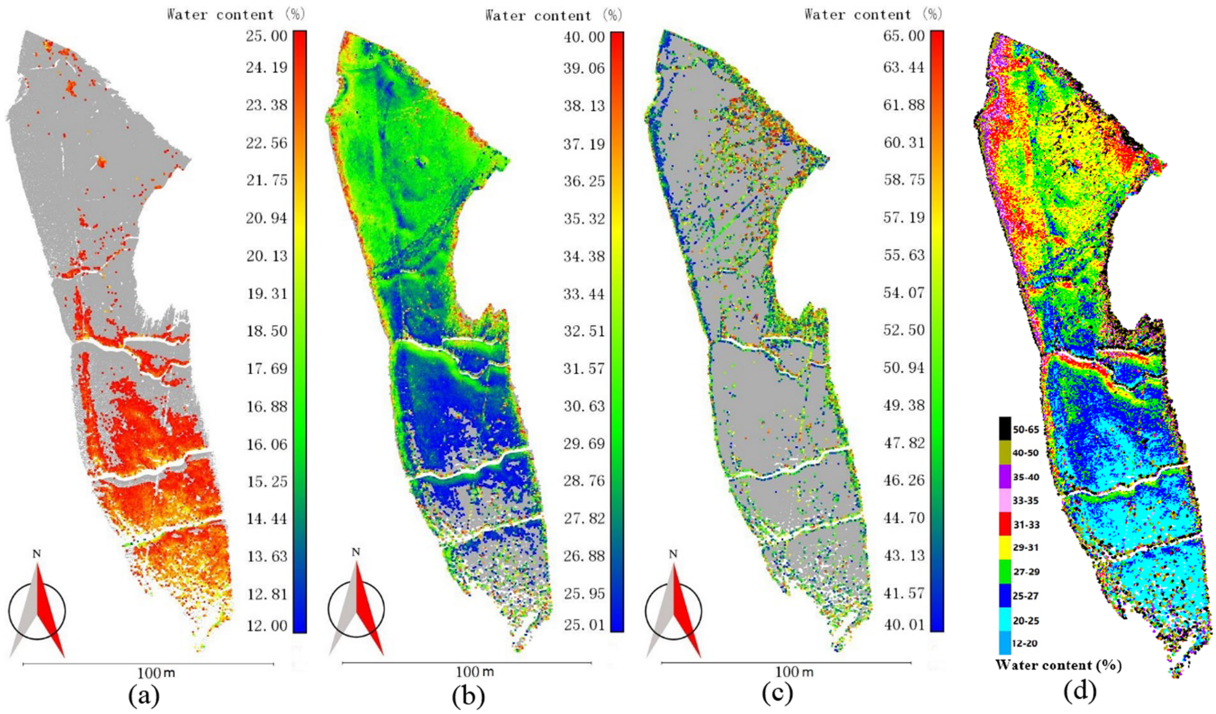

Fig. 6. Water contents estimated by corrected intensity data. (a) 12 − 25% (low), (b) 25 − 40% (middle). (c) 40 − 65% (high). (d) Water contents segmented into 10 sections.

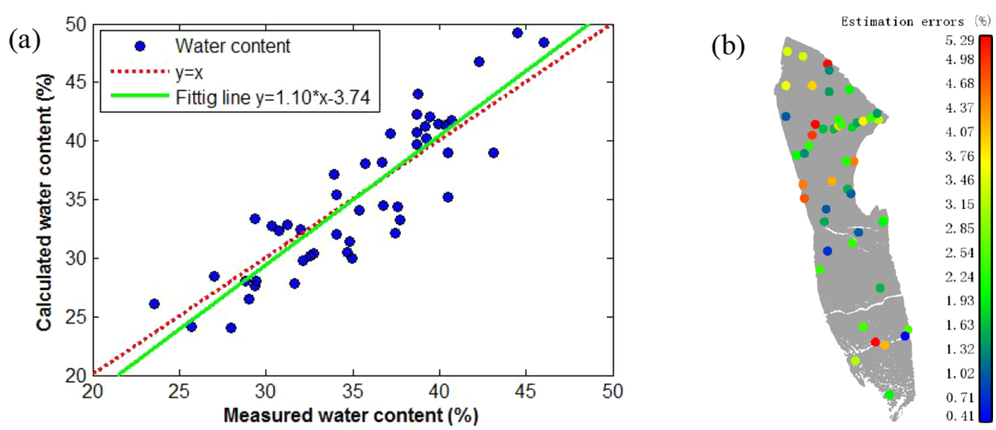

Fig. 7. (a) Relationship between the measured water contents by gravimetric method and calculated water contents by corrected intensity data for the 48 field samples. (b) Spatial distribution and water contents estimation errors for the 48 field samples.

surface laser scattering characteristics of the scanned target, and $f_2(\theta)$ should be individually estimated for different targets (Carrea et al., 2016; Kaasalainen et al., 2011; Poullain et al., 2016). The surface scattering characteristics of the cement road and mudflat are different from those of the four homogeneous targets. However, these differences are subtle because these targets can all be approximated as Lambert (Höfle and Pfeifer, 2007; Tan and Cheng, 2015). Therefore, only the dominant effects (distance and incidence angle) on the intensity data of long-range TLSs are considered in this study.

The major difference between Figs. 4(a) and 5(a) is that the intensity data of the southern part are larger than that of the northern part after correction because the original intensity data are simultaneously affected by the incidence angle and distance. The TLS instrument is positioned near the northern part (Fig. 1). Therefore, the incidence angles and distances of the northern part are smaller than those of the southern part, leading to large original intensity data of the northern part. This phenomenon suggests that the original intensity data are unreliable for water content estimation of the mudflat, and the incidence angle and distance effects must be corrected. Additionally, the intensity values of mudflat borders are both small in Figs. 4(a) and 5(a), that is, the intensity values of these regions nearly have no changes after correction. This result is due to the very high (almost saturated) water contents of these regions, and the intensity data are predominately affected by the water contents, that is, the effect of water content outweighs the effects of incidence angle and distance. Although the effects of incidence angle and distance have been eliminated after correction, the water contents of the borders are high and thus the corrected intensity data are still small.

Theoretically, when the tide begins to fall back the regions with high-elevation are the first to be exposed to air. Therefore, the high-elevation regions have more time for water evaporation than the low-elevation regions. Additionally, the water in the high-elevation regions would flow to the low-elevation regions given the effects of gravity and infiltration (He et al., 2011). Therefore, the intensity data of the high-elevation regions should be smaller than that of the low-elevation regions because of the water absorption of the laser. The original intensity

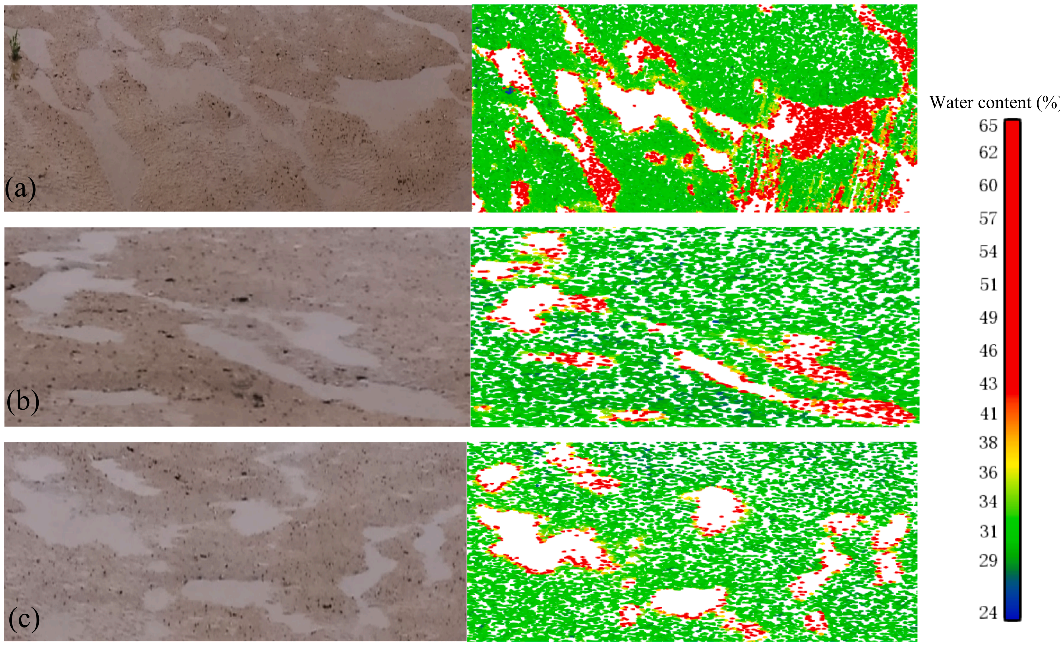

Fig. 8. Local low-lying areas with high water contents. Left: RGB images taken on site. Right: Estimated water contents. No points could be obtained in some of the regions with stagnant water because all the laser signals are absorbed by water (white areas in the right images). (a) Site 1. (b) Site 2. (c) Site 3.

data of the southern part are smaller than that of the northern part even though the elevations of the southern part are larger than that of the northern part (Fig. 4). After correction, the intensity data of the southern part are larger than that of the northern part (Fig. 5); such result is consistent with the real topography of the mudflat. This scenario suggests that the incidence angle and distance have significant influences on the intensity data. The corrected intensity data, rather than the original intensity data, can be used to estimate the water contents of the mudflat.

5.2. Mudflat scanning and water content estimation

Fig. 4(a) shows that the mudflat with an area of 300 m × 100 m can be completely scanned by only one scanning campaign using Riegl VZ-4000. The point cloud density of the regions about 300 m from the scanner at the far end of the mudflat is still approximately 5 points/m^2. Particularly, the geomorphology of the ditches could be recorded in detail (Fig. 4(a)). A number of scanning campaigns would be needed to obtain the 3D point cloud of such large mudflat if short- or middle-range TLSs are adopted. This result suggests that long-range TLSs can greatly reduce field data collection work and is highly suitable for large-area mudflats point cloud acquisition. In this study, one scanning campaign is enough to acquire the point cloud of the study mudflat. For large mudflats, the plastic reflective targets can be used to match different scanning campaigns.

The water contents of the new sample vary from 1% to 40% (Fig. 3). The new sample is almost saturated when water content reaches 40%. If more water is continually added into the new sample, then stagnant water would appear on the surface of the new sample. Therefore, the water contents of the new sample larger 40% are not investigated in this study. However, water contents from 1% to 40% are sufficient to accurately model the relationship with corrected intensity data, as indicated by the datasets of the field samples in Fig. 3. The water contents of several field samples are larger than 40% (almost saturated) because these field samples are collected from the stagnant water regions of the mudflat (e.g., the boundary between the sea and mudflat).

The 48 field samples are immediately collected when the scanning campaign of Riegl VZ-4000 is completed. The interval between the times of scanning and collecting is brief. Thus, the change in water contents for the 48 samples during this interval is subtle and can be ignored. The samples are stored in tightly sealed plastic bags. The water evaporation of the 48 samples at the interval between the times of collecting and indoor measuring could be ignored as well. Moreover, the gravimetric method measures the mean water contents of the samples with a thickness about 3–5 cm; whereas the TLS only measures the surface water contents. The water contents measured by these two methods may differ slightly (Edwards et al., 2012), and the difference is ignored in this study.

Particularly, it is noticeable that the water contents of the eastern boundary of the mudflat are very high ($40-65\%$) (Fig. 6(c)). These regions are adjacent to the land rather than the sea and should not have such high water contents. Moreover, the elevations of these regions are not low (Fig. 4(b)). The possible reason for this unexpected result is that these regions are the edges between the mudflat and vegetation (orthophoto in Fig. 1). Vegetation could prevent water evaporation, and a large amount of water is stored at the vegetation root (He et al., 2011). Therefore, vegetation distribution has a critical impact on the water contents of the mudflats. Furthermore, water contents estimated by the corrected intensity data in this study can be potentially applied to investigate the internal relationship between water contents and other quantities in mudflats, e.g., habitation of creatures and topography (see online supplementary data). These applications would be very beneficial for the ecological and environmental studies in mudflats and can lead to very interesting topics in the future.

6. Conclusions

This study proposes a new noninvasive method to rapidly and accurately estimate the water contents of intertidal mudflats using the corrected intensity data of near-infrared long-range TLSs. The proposed method significantly benefits the ecological, environmental, hydrological, and topographical studies for mudflats. Preliminary results and conclusions are obtained as follows.

(1) Incidence angle and distance significantly affect the intensity data of long-range TLSs. These two effects must be corrected to improve the accuracy and reliability of water content estimation in mudflats.

(2) The relationship between water contents and corrected intensity data can be modelled by an exponential model where the correlation-

coefficient squared is 0.98. The corrected intensity data of long-range TLSs are effective data sources for the accurate estimation of water contents of large-area intertidal mudflats with a RMSE of approximately 3%.

(3) Regions with high level water contents lie at the edges between mudflat and sea water, local low-lying areas, shores of ditches, and edges between the vegetation and mudflat. Water contents are closely related to the elevation and vegetation distribution of mudflats.

Future studies are recommended to use multitemporal long-range TLS intensity data to explore the trend of water content changes in mudflats and to deeply investigate the internal relationship among water contents and topography, vegetation distribution, and habitation of creatures. In this study, the corrected intensity data of long-range TLSs are applied to the water content estimation for a special soil type (mudflats). However, the proposed can also be applied for the estimation of water contents for other soil types, e.g., sandy beaches, desert, and inland soil. Additionally, the proposed method can be extended to water content inversions or water leakage detection for many other targets with different materials and compositions, e.g., historical buildings, rocks, underground tunnels, and tree leaves. The application of the proposed method to these targets can be very interesting and promising topics in the future.

Acknowledgments

This work is funded by Ministry of Science and Technology of the People's Republic of China under Grant 2017YFE0107400, Science and Technology Commission of Shanghai Municipality under Grant 18DZ1206401, National Natural Science Foundation of China under Grants 41901399 and 41671449, State Key Laboratory of Estuarine and Coastal Research, East China Normal University under Grants 2017RCDW06 and 2017TASK06, State Laboratory of Information Engineering in Surveying, Mapping and Remote Sensing, Wuhan University under Grant 19S02, Key Laboratory of Surveying and Mapping Science and Geospatial Information Technology of Ministry of Natural Resources under Grant 201916, Shanghai Sailing Program under Grant 18YF1406800, China Postdoctoral Science Foundation under Grant 2017M620141, and Guangzhou Municipal Science and Technology Bureau under Grant 201704030102. The authors would like to thank Guoan Zhang, Shengzu Zhu, Zhonghao Zhao, Bowen You, Xiaohui Chen, and Lixin Qiao from the State Key Laboratory of Estuarine and Coastal Research in East China Normal University for helping field data collecting.

Appendix A. Supplementary material

Supplementary data to this article can be found online at https://doi.org/10.1016/j.isprsjprs.2019.11.003.

References

Andriolo, U., Almeida, L.P., Almar, R., 2018. Coupling terrestrial LiDAR and video imagery to perform 3D intertidal beach topography. Coast. Eng. 140, 232–239.

Brakenhoff, L.B., Smit, Y., Donker, J.J., Ruessink, G., 2019. Tide-induced variability in beach surface moisture: Observations and modelling. Earth Surf. Proc. Land. 44 (1), 317–330.

Carrea, D., Abellan, A., Humair, F., Matasci, B., Derron, M.H., Jaboyedoff, M., 2016. Correction of terrestrial LiDAR intensity channel using Oren-Nayar reflectance model: an application to lithological differentiation. ISPRS J. Photogramm. Remote Sens. 113, 17–29.

Choe, B.H., Kim, D.J., Hwang, J.H., Oh, Y., Moon, W.M., 2012. Detection of oyster habitat in tidal flats using multi-frequency polarimetric SAR data. Estuar. Coast. Shelf Sci. 97, 28–37.

Darke, I., Davidson-Arnott, R., Ollerhead, J., 2009. Measurement of beach surface moisture using surface brightness. J. Coast. Res. 248–256.

Donker, J., van Maarseveen, M., Ruessink, G., 2018. Spatio-temporal variations in foredune dynamics determined with mobile laser scanning. J. Mar. Sci. Eng. 6 (4), 126.

Edwards, B.L., Namikas, S.L., D'sa, E.J., 2013. Simple infrared techniques for measuring beach surface moisture. Earth Surf. Proc. Land 38 (2), 192–197.

Edwards, B.L., Schmutz, P.P., Namikas, S.L., 2012. Comparison of surface moisture measurements with depth-integrated moisture measurements on a fine-grained beach. J. Coast. Res. 29 (6), 1284–1291.

Eisma, D., 1998. Intertidal Deposits: River Mouths, Tidal Flats, and Coastal Lagoons (vol. 16). CRC Press.

Fabbri, S., Giambastiani, B.M., Sistilli, F., Scarelli, F., Gabbianelli, G., 2017. Geomorphological analysis and classification of foredune ridges based on terrestrial laser scanning (TLS) technology. Geomorphology 295, 436–451.

Fang, W., Huang, X., Zhang, F., Li, D., 2014. Intensity correction of terrestrial laser scanning data by estimating laser transmission function. IEEE Trans. Geosci. Remote Sens. 53 (2), 942–951.

Franceschi, M., Teza, G., Preto, N., Pesci, A., Galgaro, A., Girardi, S., 2009. Discrimination between marls and limestones using intensity data from terrestrial laser scanner. ISPRS J. Photogramm. Remote Sens. 64 (6), 522–528.

Guisado-Pintado, E., Jackson, D.W., Rogers, D., 2019. 3D mapping efficacy of a drone and terrestrial laser scanner over a temperate beach-dune zone. Geomorphology 328, 157–172.

He, Y., Li, X., Craft, C., Ma, Z., Sun, Y., 2011. Relationships between vegetation zonation and environmental factors in newly formed tidal marshes of the Yangtze River estuary. Wetlands Ecol. Manage. 19 (4), 341–349.

Höfle, B., Pfeifer, N., 2007. Correction of laser scanning intensity data: data and model-driven approaches. ISPRS J. Photogramm. Remote Sens. 62 (6), 415–433.

Kaasalainen, S., Krooks, A., Kukko, A., Kaartinen, H., 2009. Radiometric calibration of terrestrial laser scanners with external reference targets. Remote Sens. 1 (3), 144–158.

Kaasalainen, S., Jaakkola, A., Kaasalainen, M., Krooks, A., Kukko, A., 2011. Analysis of incidence angle and distance effects on terrestrial laser scanner intensity: search for correction methods. Remote Sens. 3 (10), 2207–2221.

Kashani, A., Olsen, M., Parrish, C., Wilson, N., 2015. A review of LiDAR radiometric processing: from ad hoc intensity correction to rigorous radiometric calibration. Sensors 15 (11), 28099–28128.

Le Hir, P., Roberts, W., Cazaillet, O., Christie, M., Bassoullet, P., Bacher, C., 2000. Characterization of intertidal flat hydrodynamics. Cont. Shelf Res. 20 (12–13), 1433–1459.

Li, H., Gong, Z., Dai, W., Lu, C., Zhang, X., Cybele, S., Guo, H., 2018. Feasibility of elevation mapping in muddy tidal flats by remotely sensed moisture (RSM) method. J. Coast. Res. 85 (sp1), 291–295.

Nahon, A., Molina, P., Blázquez, M., Simeon, J., Capo, S., Ferrero, C., 2019. Corridor mapping of sandy coastal foredunes with UAS photogrammetry and mobile laser scanning. Remote Sens. 11 (11), 1352.

Nguyen, C., Starek, M., Tissot, P., Gibeaut, J., 2018. Unsupervised clustering method for complexity reduction of terrestrial lidar data in marshes. Remote Sens. 10 (1), 133.

Nield, J.M., Wiggs, G.F., Squirrell, R.S., 2011. Aeolian sand strip mobility and protodune development on a drying beach: Examining surface moisture and surface roughness patterns measured by terrestrial laser scanning. Earth Surf. Proc. Land. 36 (4), 513–522.

Nield, J.M., Wiggs, G.F., 2011. The application of terrestrial laser scanning to aeolian saltation cloud measurement and its response to changing surface moisture. Earth Surf. Proc. Land. 36 (2), 273–278.

Nield, J.M., King, J., Jacobs, B., 2014. Detecting surface moisture in aeolian environments using terrestrial laser scanning. Aeolian Res. 12, 9–17.

Nolet, C., Poortinga, A., Roosjen, P., Bartholomeus, H., Ruessink, G., 2014. Measuring and modeling the effect of surface moisture on the spectral reflectance of coastal beach sand. PLoS ONE 9 (11), e112151.

Oblinger, A., Anthony, E.J., 2008. Surface moisture variations on a multibarred macrotidal beach: Implications for aeolian sand transport. J. Coast. Res. 1194–1199.

Phang, V.X., Chou, L.M., Friess, D.A., 2015. Ecosystem carbon stocks across a tropical intertidal habitat mosaic of mangrove forest, seagrass meadow, mudflat and sandbar. Earth Surf. Proc. Land. 40 (10), 1387–1400.

Poullain, E., Garestier, F., Levoy, F., Bretel, P., 2016. Analysis of ALS intensity behavior as a function of the incidence angle in coastal environments. IEEE J. Sel. Top. Appl. Earth Obs. Remote Sens. 9 (1), 313–325.

Rajput, P., Ramakrishnan, R., Rajawat, A.S., 2018. Geomorphological study of intertidal mudflats using RISAT-1 SAR images. Remote Sens. Lett. 9 (12), 1128–1137.

Schmutz, P.P., Namikas, S.L., 2011. Utility of the Delta-T Theta Probe for obtaining surface moisture measurements from beaches. J. Coast. Res. 27 (3), 478–484.

Schmutz, P.P., Namikas, S.L., 2018. Measurement and modeling of the spatiotemporal dynamics of beach surface moisture content. Aeolian Res. 34, 35–48.

Smit, Y., Donker, J.J., Ruessink, G., 2019. Spatiotemporal surface moisture variations on a barred beach and their relationship with groundwater fluctuations. Hydrology 6 (1), 8.

Smit, Y., Ruessink, G., Brakenhoff, L.B., Donker, J.J., 2018. Measuring spatial and temporal variation in surface moisture on a coastal beach with a near-infrared terrestrial laser scanner. Aeolian Res. 31, 19–27.

Suchocki, C., Katzer, J., 2018. Terrestrial laser scanning harnessed for moisture detection in building materials–Problems and limitations. Autom. Constr. 94, 127–134.

Tan, K., Cheng, X., 2015. Intensity data correction based on incidence angle and distance for terrestrial laser scanner. J. Appl. Remote Sens. 9 (1), 094094.

Tan, K., Cheng, X., Ju, Q., Wu, S., 2016. Correction of mobile TLS intensity data for water leakage spots detection in metro tunnels. IEEE Geosci. Remote Sens. Lett. 13 (11), 1711–1715.

Tan, K., Cheng, X., 2016. Correction of incidence angle and distance effects on TLS intensity data based on reference targets. Remote Sens. 8 (3), 251.

Tan, K., Chen, J., Qian, W., Zhang, W., Shen, F., Cheng, X., 2019. Intensity data correction for long-range terrestrial laser scanners: a case study of target differentiation in an intertidal zone. Remote Sens. 11 (3), 331.

Telling, J., Lyda, A., Hartzell, P., Glennie, C., 2017. Review of Earth science research

using terrestrial laser scanning. Earth Sci. Rev. 169, 35–68.
Wang, Y.P., Gao, S., Jia, J., Thompson, C.E., Gao, J., Yang, Y., 2012. Sediment transport over an accretional intertidal flat with influences of reclamation, Jiangsu coast, China. Mar. Geol. 291, 147–161.
Wiggs, G.F.S., Baird, A.J., Atherton, R.J., 2004. The dynamic effects of moisture on the entrainment and transport of sand by wind. Geomorphology 59 (1–4), 13–30.
Xie, W., He, Q., Zhang, K., Guo, L., Wang, X., Shen, J., Cui, Z., 2017. Application of terrestrial laser scanner on tidal flat morphology at a typhoon event timescale. Geomorphology 292, 47–58.
Xu, T., Xu, L., Li, X., Yao, J., 2018. Detection of water leakage in underground tunnels using corrected intensity data and 3D point cloud of terrestrial laser scanning. IEEE Access 6, 32471–32480.
Xu, T., Xu, L., Yang, B., Li, X., Yao, J., 2017. Terrestrial laser scanning intensity correction by piecewise fitting and overlap-driven adjustment. Remote Sens. 9 (11), 1090.
Yang, Y., Davidson-Arnott, R.G., 2005. Rapid measurement of surface moisture content on a beach. J. Coast. Res. 447–452.
Yan, W.Y., Shaker, A., 2014. Radiometric correction and normalization of airborne LiDAR intensity data for improving land-cover classification. IEEE Trans. Geosci. Remote Sens. 52 (12), 7658–7673.
Zhu, X., Wang, T., Darvishzadeh, R., Skidmore, A.K., Niemann, K.O., 2015. 3D leaf water content mapping using terrestrial laser scanner backscatter intensity with radiometric correction. ISPRS J. Photogramm. Remote Sens. 110, 14–23.